Nanoscale Advances

ROYAL SOCIETY OF CHEMISTRY

PAPER

View Article Online
View Journal | View Issue

Cite this: *Nanoscale Adv.*, 2025, **7**, 4087

Polymer/AgPt bimetallic nanoparticle synergy: optimizing plasmonic durability through controlled synthesis and matrix integration†

Abeer Fahes, *[a] Lavinia Balan, [b] Caroline Andreazza-Vignolle, [a] Claudia de Melo, [a] Didier Zanghi[b] and Pascal Andreazza *[a]

An innovative approach combining UV-induced polymerization and ultra-high vacuum (UHV) atomic vapor deposition was developed to synthesize and disperse 2–3 nm AgPt bimetallic nanoparticles (BNPs) within a non-porous poly (dipropylene glycol diacrylate) (PDGDA) matrix, surpassing conventional porous polymer strategies. This method offers unprecedented control over the structural properties of BNPs and in general nanoalloys, with the polymer matrix playing a critical role in regulating nanoparticle formation, spatial arrangement, and size uniformity. The PDGDA matrix enhances nanoparticle stability through steric stabilization and controlled diffusion, effectively maintaining small nanoparticle sizes (~2.4–2.8 nm) and low dispersity (σ_D/D = 0.16) during extended high-temperature annealing. Confinement of nanoparticles (NPs) was significantly accelerated by successive thermal annealing to 320 °C, which increased polymer chain mobility and reduced viscosity, enabling rapid diffusion while preserving the structural integrity of the polymer matrix. This process dramatically reduced the embedding time from 12 days at room temperature to near-instantaneous incorporation upon heating. Successful confinement is attributed to key thermodynamic factors that promote interfacial interactions and particle mobility within the polymer network. Experimental results reveal distinctive UV plasmonic properties of the embedded AgPt BNPs with long-term stability. The produced AgPt BNPs exhibit significantly stronger localized surface plasmon resonances (LSPRs) than pure platinum nanoparticles, attributed to synergistic effects between the two metals. Factors contributing to this enhancement include silver's high electrical conductivity and relatively low optical losses, electromagnetic coupling, and localized electric field enhancement, highlighting the potential of these BNPs for advanced plasmonics. This research addresses the growing demand for surface-enhanced Raman scattering (SERS) detection of UV-absorbing biospecies and the development of more efficient broad-spectrum solar cells.

Received 25th February 2025
Accepted 7th May 2025

DOI: 10.1039/d5na00187k

rsc.li/nanoscale-advances

Introduction

The combination of polymers and nanoparticles (NPs) yields highly intriguing and functional materials due to the mutualistic benefits derived from their coexistence.[1,2] Bimetallic nanostructures, particularly in nanoalloy configurations, exhibit remarkable characteristics distinct from pure monometallic structures and basic physical mixtures, showcasing a unique synergy that enhances their overall performance and functionality.[3,4] Incorporating bimetallic nanoparticles (BNPs) into polymer films facilitates their immobilization and organization, enabling the adjustment of electronic, optical, sensing, and catalytic properties *via* the dielectric environment.[5,6] This integration not only improves the responses of NPs but also influences the intrinsic material properties of the polymer matrix. Over the past decade, there has been significant progress in extending synthetic protocols for these systems.[7–9]

The localized surface plasmon resonance (LSPR) phenomenon is heavily influenced by the particle's composition, size, shape, and interparticle distances, as well as the surrounding dielectric medium, due to its reliance on spatial fluctuations and surface electron density.[10,11] Plasmonic coupling is responsible for one of the most compelling optical phenomena; the strong amplification of electromagnetic fields at the interparticle junctions, known as hotspot regions, offers exceptional potential for diverse sensing technologies.[12] While nanoplasmonics have predominantly been studied in noble metal nanostructures larger than 5 nm within the near-infrared to visible range,[13–16] emerging applications necessitate extending this study to higher energies, particularly in the near-UV region. This shift toward the UV region is driven by the need for enhanced detection of biospecies with UV absorption bands

[a]*Université d'Orléans, CNRS, ICMN, UMR 7374, Orléans, France. E-mail: abeer.fahes@cnrs-orleans.fr; pascal.andreazza@univ-orleans.fr*

[b]*Université d'Orléans, CNRS, CEMHTI, UPR 3079, Orléans, France*

† Electronic supplementary information (ESI) available. See DOI: https://doi.org/10.1039/d5na00187k

(such as nucleotide bases and aromatic amino acids below 350 nm) and the development of more efficient broad-spectrum solar cells and photovoltaic devices that can harness UV light, thus opening new avenues in biosensing and renewable energy technologies.[17,18]

However, transitioning to UV plasmonics with sub-5 nm polymer/nanoalloys presents challenges. Plasmon resonances can be observed only over a restricted wavelength range (a few tens of nm) by varying nanoparticle sizes in spheroidal shapes.[19] Plasmonic red-shift is maximized when nanostructures are positioned in extremely close proximity (strong near-field coupling) and when two distinct metals are coupled within a single configuration.[20] As NPs approach the sub-5 nm size regime, their weak scattering and increased sensitivity to surface phenomena and chemical environments become more pronounced, significantly influencing their plasmonic behavior.[21] In LSPR, strong and localized electromagnetic fields affect NPs, causing modifications in extinction and scattering spectra in response to even minor changes in the refractive index.[11] This can result from various surface morphological characteristics, including roughness, defects, lattice shrinkage, residual surfactants, porosity, ligands, surface oxides, adhesion layers, or interactions with the supporting substrate.[21,22] For instance, as a general principle, the porosity of the polymer matrix introduces irregularities on the nanoparticle surface, increasing electron scattering and energy loss, broadening the plasmon resonance peaks, and reducing their intensity.[23] Achieving a uniform plasmonic response in nanoalloys is hindered by compositional inhomogeneities and surface segregation, where elements unevenly distribute throughout the material and potentially concentrate at surfaces, leading to inconsistent electronic properties and localized differences in plasmonic behavior.[24]

Many conventional and built-up optical setups are flawed in terms of their spatial and spectral resolution and detection ranges, hindering the study of plasmonic properties.[23–25] To overcome these obstacles, advanced characterization techniques, UV-compatible optics, and detection systems capable of accurately interpreting the plasmonic behavior of these sub-5 nm nanoalloys, while considering surface and environmental effects and metal types, must be developed. For example, LSPR peaks are poorly defined in metals with low-quality factors (such as platinum (Pt)), making them ineffective for plasmonic applications.[26] By integrating silver (Ag) and Pt NPs in a nanoalloy configuration, this issue can be resolved, leveraging Ag's high plasmonic strength and strong photon interaction across the UV-Vis-NIR spectrum along with UV-Pt's superior chemical stability, resulting in well-defined LSPR peaks.[27]

Plasmon damping, characterized by reduced resonance efficiency, is a major factor contributing to the deterioration of optical properties.[28] Therefore, robust stabilization strategies are necessary to ensure performance stability while preserving intrinsic plasmonic properties.[29] Without suitable stabilizers, AgPt BNPs may oxidize, aggregate or segregate, ultimately losing their plasmonic properties over time. Confined NPs in a non-porous polymer matrix offer a practical solution to this problem. This method represents an alternative to porous polymer/NPs composites, involving the *in situ* synthesis of metal NPs inside a porous polymer film. There is still much to explore regarding non-porous polymer–nanoparticle composites, including manufacturing processes and potential applications. Porous polymer structures have traditionally been favored for NP embedding due to their enhanced surface area and templating capabilities. However, this work demonstrates that effective NP confinement can be achieved in non-porous polymer matrices, where the polymer matrix and NPs are formed separately, challenging the conventional reliance on porous structures.[30] By expanding the scope of NP embedding techniques, polymer/NPs composites can be tailored to meet specific properties, broadening their range of applications.

This paper presents an overview of a preliminary attempt to create hybrid materials with unique properties by depositing an organic component, typically a polymer or monomer, onto Si/SiO_2 surfaces through a photochemical process. This initial layer is then coated with a discontinuous layer of AgPt using atomic vapor deposition. This innovative approach combines two complementary methods, ultimately paving the way for the development of advanced materials with tailored characteristics. The photoinduced method allows for the rapid generation of a poly(dipropylene glycol diacrylate) (PDGDA) polymer layer within minutes of UV exposure, utilizing solvent-free monomers at room temperature (RT) and at low cost. This represents a clear improvement over traditional polymerization methods, offering many advantages such as fast curing, interconnected polymer production, and low energy consumption.[31] Meanwhile, atomic vapor deposition leads to the controlled growth of discontinuous films through continuous atomic flux during growth, resulting in moderate kinetic energy, low polydispersity of NP assemblies, and a high throughput of NPs.[32,33] To date, atomic vapor deposition has been limited to only monometallic (Ag or Pt)[34] and BNPs (*e.g.*, CoAg,[35] AgPt,[36] CoPt,[37] AgAl,[29] and AgIn[29]) on silica matrices, but strategies for creating long-term stable nanocomposites with durable structural and optical properties remain underdeveloped.

As part of our primary goals, we aim to minimize polydispersity in NP size and interparticle spacing, stabilize NPs within polymeric matrices, and detect their UV plasmonic properties, with a key fabrication consideration being the uniform distribution of NPs and the variable degrees of insertion into the matrix. Analyzing the NPs within the polymer matrix through appropriate microscopy and spectroscopy methods is a crucial practical aspect. This investigation explores the interplay of several factors: (i) the presence or absence of a polymer matrix, (ii) the bimetallic nanoalloying of AgPt *versus* monometallic NPs (Ag, Pt), and (iii) the influence of annealing (ranging from RT to 320 °C). A thorough understanding of how these variables affect the properties and behavior of NP systems is provided. Complementary experimental techniques (detailed in the ESI†), such as Grazing Incidence Small Angle X-ray Scattering (GISAXS), Rutherford Backscattering Spectrometry (RBS), X-ray Photoelectron Spectroscopy (XPS), Transmission Electron Microscopy (TEM), Scanning Electron Microscopy (SEM), UV/Vis spectroscopy, ellipsometry, profilometry, and Fourier Transform Infrared Spectroscopy (FTIR), have been

indispensable in unequivocally characterizing these complex polymer/NPs nanocomposite systems.

Experimental section

Synergistic nanoengineering: polymer/AgPt bimetallic nanocomposites

Photo-induced synthesis of the polymer matrix. A polymer film was developed using a photoinduced polymerization technique, as shown in Fig. 1(a). The GISAXS 2D pattern presented in Fig. S1† confirms the absence of porosity in the polymer film. The process utilized a formulation composed of dipropylene glycol diacrylate as the monomer, with 2% of 2-hydroxy-2-methyl-1-phenyl-propan-1-one serving as the photoinitiator for free radical generation. A diacrylate monomer was chosen for its high reactivity, fast polymerization, moderate viscosity, and excellent diffusion, enabling efficient copolymerization and high conversion rates. The mixture was subsequently deposited onto a pre-cleaned boron-doped Si/SiO_2 substrate with dimensions of 1×1 cm^2 and a 2 nm thick oxide layer using spin-coating methodology. The resulting film achieved a thickness of 7 μm using a POLOS SPIN150i spin coater, with the following optimized parameters: spin speed of 2000 rpm, acceleration of 1000 rpm, and duration of 10 s. The thickness and roughness of the polymer layer were determined using interferometric profilometry (Fig. 1(a)), a non-contact optical technique that analyzes interference fringes to measure surface height variations with high precision, without damaging the sample. The acceleration value (1000 rpm) was set lower than the spin-coating speed (2000 rpm) to form a homogeneous layer and improve the reproducibility of layer thickness across multiple sample preparations. A spin-coating duration of 10 s was found to be optimal for enhancing the spreading of the polymer layer, leading to improved film uniformity, dispersion stability, and consistent coverage across the substrate.

The photochemical synthesis was initiated using a Hamamatsu Lightningcure LC8 (Hg–Xe L8252) UV source operating at

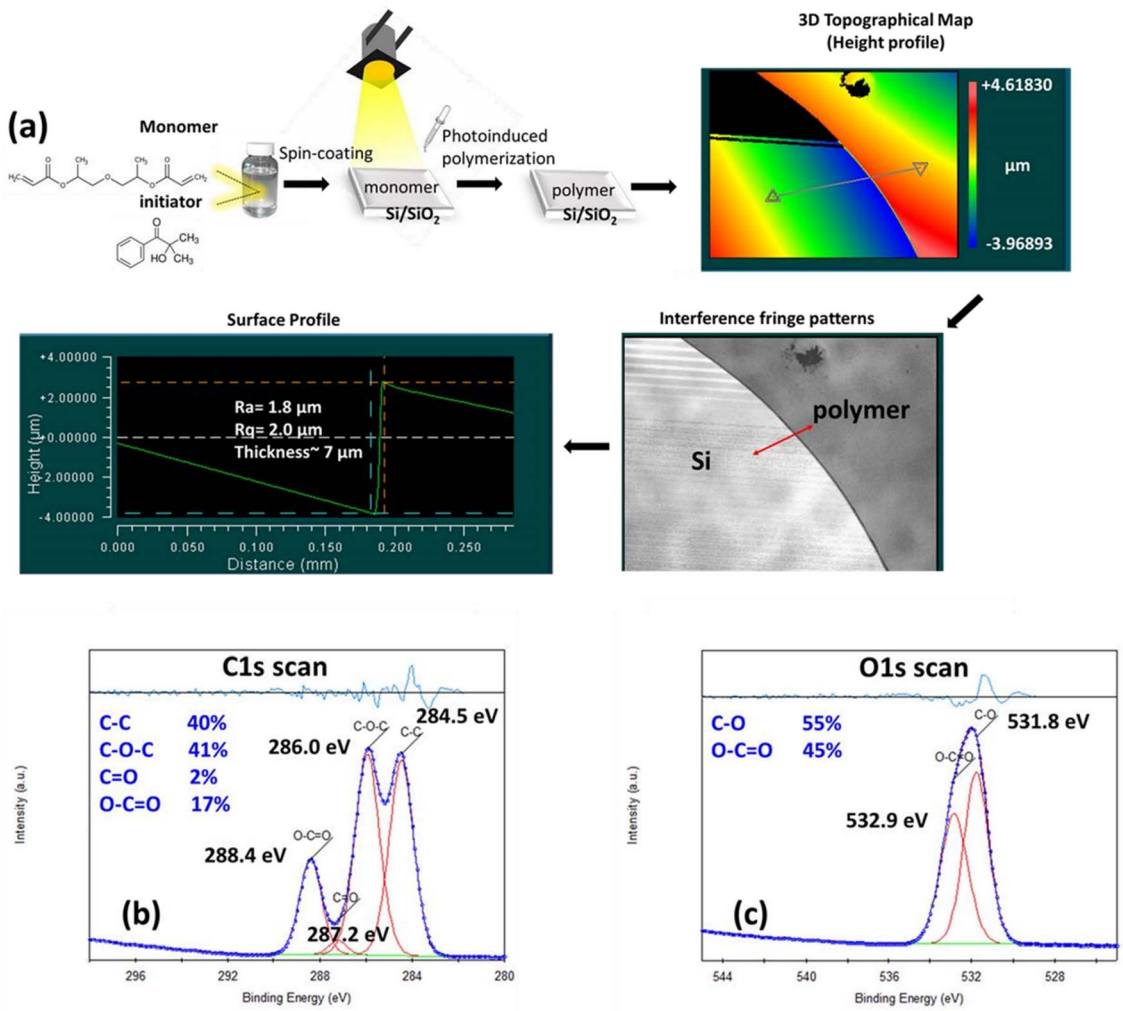

Fig. 1 (a) Schematic illustration of the photoinduced polymerization process with the corresponding interferometric profilometry results, including 3D topographical mapping, interference fringe patterns, and surface profile analysis for thickness and roughness (average surface roughness (R_a) and root mean square roughness) estimation, and (b and c) deconvoluted XPS C 1s and O 1s core-level spectra of the polymer film.

365 nm. The sample was positioned horizontally at a distance of 13 cm from the lamp, ensuring uniform UV exposure over the entire surface. A fluence of 360 mW cm^{-2} was applied for 2 min, achieving a polymer conversion rate of 73%. This conversion rate was quantified by monitoring the reduction of the characteristic C=C acrylate double bond peak at 1636 cm^{-1} using FTIR spectroscopy.[38]

Ultra-high vacuum (UHV) atomic vapor deposition of BNPs. A discontinuous thin layer of Ag/Pt nanoalloys (~1 nm of equivalent thickness), with mean sizes ~2–3 nm, was then deposited onto the PDGDA film at RT to facilitate the embedding of NPs within the polymer matrix. The deposition process was conducted in a molecular beam deposition (MBE) set-up in an UHV environment, maintained at a pressure of 10^{-10} mbar, to ensure optimal conditions for film growth. This low pressure served two critical purposes: firstly, it minimized the risk of contamination from residual gases, preserving the purity of the deposited material; secondly, it significantly extended the mean free path of evaporated atoms. The latter aspect was crucial for maintaining precise control over the flux and directionality of molecular beams, which directly influence the uniformity, reproducibility, and quality of the thin films.

We adopted a methodological framework closely aligned with the principles outlined in this review.[33] Ag and Pt metallic sources were evaporated *via* electron beam bombardment, and the triggered atomic beams were directed towards a polymer substrate positioned ~100 mm from the metal targets.[34] The compositional ratios of the formed Ag/Pt NPs were precisely controlled by modulating the atomic flux applied to each metal target during the atomic flux regulation stage of MBE, achieved by systematically adjusting the electron energy to the target through voltage variation while maintaining fixed filament currents ($I_{filament}$) of 1.85 A for Ag and 2.6 A for Pt sources. A constant deposition rate of 0.4×10^{15} atoms per cm^2 per h was maintained for both Ag and Pt to reach 50 : 50 Ag : Pt composition. This low deposition rate was chosen to favor the equilibrium conditions of atom deposition and diffusion on the polymer matrix. The deposition process leads to a total deposited atomic amount of $(5.2 \pm 0.3) \times 10^{15}$ atoms per cm^2, as corroborated by RBS post-deposition analysis.

Results and discussion

From monomer to polymer matrix: integrative methods for acrylic polymer systems

XPS deconvolution of the C 1s and O 1s spectra, as highlighted in Fig. 1(b) and (c), reveals the presence of various chemical groups within the polymer structure, including C–C, C=O, O–C=O, and C–O–C. However, the XPS results alone were insufficient to definitively determine whether a partial or full polymerization had occurred. For this reason, FTIR measurements were conducted to quantify the degree of conversion. The results, as shown in Fig. 2(b), indicate a 73% conversion of C=C into C–C bonds. The absence of any detectable C=C bonds in the XPS spectra, despite the incomplete polymerization indicated by FTIR, can be attributed to the low concentration of residual unreacted monomers in the material. Accordingly, C=C bonds at the surface are below the detection limit of XPS and, unlike FTIR, XPS cannot accurately reflect the bulk material composition.

It is worth noting that the observed C 1s binding energy at 284.5 eV in the polymer reflects a 0.3 eV shift from the standard adventitious carbon reference (284.8 eV), which we attribute to two main factors: (1) the high interconnection density of the

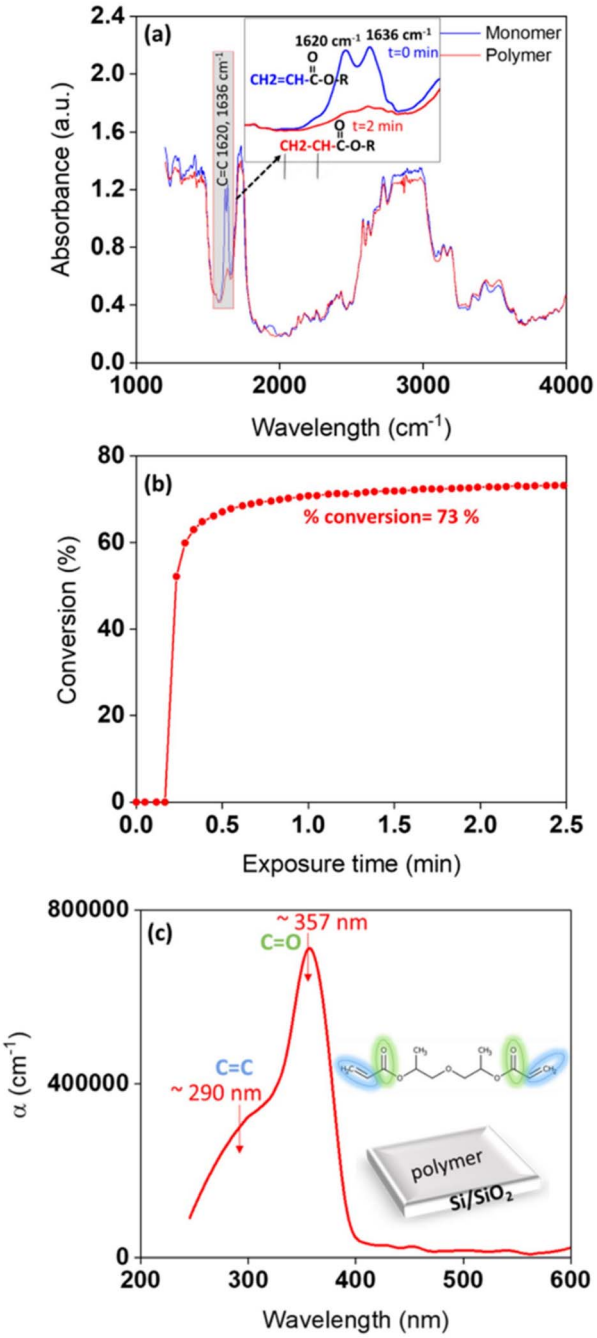

Fig. 2 (a) Comparative infrared spectral analysis of acrylic formulation: pre- (at $t = 0$ min) and post- (at $t = 2$ min) polymerization, (b) real-time FTIR kinetics of UV-induced acrylic polymerization at $\lambda = 365$ nm, and (c) ellipsometric determination of the absorption coefficient (α) in UV-cured acrylic polymer films.

PDGDA matrix, which slightly reduces the electron density at carbon sites, and (2) residual charging effects inherent to insulating polymer systems, despite calibration and active flood gun compensation during measurement.[39]

Deconvolution of the C 1s spectra revealed five distinct peaks in the monomer (including a C=C component at 284.1 eV; see Fig. S2†), which were reduced to four in the polymer. The polymer's C 1s XPS spectrum exhibits a single peak at 284.5 eV, assigned exclusively to C–C (sp^3) bonding, for two key reasons. First, FTIR analysis (Fig. 2(a) and (b)) shows the near-complete disappearance of C=C stretching modes, confirming the consumption of sp^2 carbon during polymerization. Second, while the monomer spectrum shows distinct peaks at 284.1 eV (C=C) and 285.1 eV (C–C), the polymer spectrum does not display any clear component below 284.5 eV. The lack of peak splitting or visible shoulders in the polymer spectrum, along with the 0.6 eV shift from the monomer's C–C peak (285.1 eV), is consistent with minor charging effects in highly interconnected insulating polymers rather than the presence of sp^2 carbon.

Polymer chain interconnection is evident in Fig. 2(a), where the FTIR spectrum of the polymer shows significantly reduced C=C absorption bands at 1620 and 1636 cm^{-1}. The well-documented FTIR spectral assignments of poly (ethylene glycol diacrylate) (PEGDA) provide a reliable reference for interpreting PDGDA spectra, given the structural similarities between these polymers.[40–45] The peaks observed in the 3300–3600 cm^{-1} region are associated with O–H stretching vibrations, likely due to residual unreacted hydroxyl groups from the starting materials.[44,45] This observation confirms that the polymerization rate is consistent with 73% for PDGDA under these conditions.

Fig. 2(b) shows that the reaction begins rapidly, with detectable polymerization occurring within 13 s (0.223 min) of UV exposure. This prompt onset is attributed to the efficient generation of free radicals by the photo-initiator and the high reactivity of the acrylate groups. The polymerization proceeds swiftly, nearing completion within 53 s (0.883 min) of UV irradiation. The polymerization reaction reaches a steady state after 2 min of continuous UV irradiation, indicating the formation of a stable, interconnected polymer network. The attainment of a 73% conversion plateau marks the end of the polymerization process under the given conditions, with approximately one-quarter of the monomers remaining unreacted.

Fig. 2(c) shows the absorption coefficient of the polymer film, revealing two characteristic electronic transitions in the UV region. This spectral profile reflects the polymer's molecular structure and polymerization dynamics.[46] The peak at 290 nm corresponds to the π–π^* transition of C=C bonds in acrylate groups, while the more prominent peak at 357 nm represents the n–π^* transition of carbonyl (C=O) groups. Typically, in the literature, n–π^* transitions are less intense than π–π^* transitions due to their weaker absorption.[47,48] However, in this case, this difference is not surprising, as the intensity ratio of these peaks reflects the polymerization process. During the reaction, C=C bonds are consumed, while C=O groups remain unaffected, which results in the enhanced relative intensity of the n–π^* transition.

Tailoring nanostructures: interplay between polymer matrices and bimetallic nanoalloying

Table 1 summarizes the key attributes across different NP types and matrix materials. To elucidate the influence of a polymer matrix, two comparative sample sets were fabricated: one incorporating a polymer matrix and a control set without the matrix. The substrate surface plays a critical role in perturbing the nucleation process, primarily due to low-energy sites such as chemical surface defects, adsorbed impurities, or topologically favorable sites. Additionally, factors, such as sticking and diffusion coefficients, and the strength of substrate–adsorbate interactions, are also influential.[33] The Ag and/or Pt metal deposition induces the formation of isolated NPs that are characteristic of island-type nucleation and growth as in the Volmer–Weber (VW) growth mode.[49]

GISAXS analysis demonstrates that the matrix has no noticeable impact on the nanoparticle diameter (D) or the height-to-diameter aspect ratio (H/D), suggesting that nanoparticle growth is predominantly governed by the intrinsic properties of the AgPt nanoalloy rather than by strong substrate interactions. The observed H/D ratio approaching 1 (~0.9–0.95) aligns with the Wulff-polyhedron theory, which describes metal–support affinity, indicating minimal metal nanoparticle–substrate interactions for both silica and polymer substrates.[40] The presence of the polymer matrix substantially reduces polydispersity in both size and interparticle distance distributions, concurrently decreasing mean interparticle distances (Λ). These findings indicate that the polymer matrix plays an important role in regulating nanoparticle spatial arrangement and size uniformity, likely *via* mechanisms such as steric stabilization, controlled diffusion, and confined growth.

The correlation between increased size distribution and high interparticle distances in the Si/AgPt sample with a comparable

Table 1 Attributes, including NP diameter (D), height-to-diameter aspect ratio (H/D), inter-particle spacing (Λ), size and interparticle distribution parameters (σ_D/D and w), of mono- and bimetallic NPs in polymer and silica matrices deduced from GISAXS simulations. The inverse formulation $\Lambda \approx 2\pi/q_y$ is indeed a first approximation for interparticle distances in GISAXS that estimates the average interparticle distances from the position of features in the q_y scattering profile. However, simulations can consider two key factors: form factor (NPs shape) and interference function (distribution of the NP assembly) and consequently the average interparticle distance and the degree of positional disorder among NPs

Sample at RT	D (nm)	σ_D/D	H/D	$\Lambda \approx 2\pi/q_y$ (nm)	w (nm)
Si/polymer/AgPt	2.4 ± 0.04	0.17	0.95 ± 0.01	3.6 ± 0.1	1.0
Si/polymer/Ag	3.2 ± 0.04	0.15	0.90 ± 0.01	5.7 ± 0.1	1.7
Si/polymer/Pt	2.2 ± 0.04	0.14	0.95 ± 0.01	3.0 ± 0.1	0.8
Si/AgPt	2.4 ± 0.04	0.25	0.90 ± 0.01	4.8 ± 0.1	1.4

mean diameter to Si/polymer/AgPt can be attributed to the heterogeneous spatial distribution of particles, where larger NPs occupy more space, forcing smaller ones further apart, resulting in fewer particles per unit area while maintaining the same overall volume fraction of the material.

Surface roughness and electronic contrast variations influence GISAXS scattering intensity.[50] The profilometry data in Fig. 1(a) show that the polymer layer has significant surface roughness, which is much greater than that of the typically smooth Si/SiO_2 substrates. This high roughness of the polymer reduces the GISAXS intensity compared to smoother surfaces.

The polymer's lower density ($\rho_{polymer} = 1.05$ g cm^{-3}) relative to SiO_2 ($\rho_{SiO_2} = 2.65$ g cm^{-3}),[51] directly related to the electron density, leads to reduced scattering intensity. These factors become evident when comparing the scattering profiles of Si/AgPt and Si/polymer/AgPt systems as shown in Fig. 3(a) and (b). Furthermore, in the context of mono- and bimetallic NPs deposited on the polymer matrix, we observe that Ag exhibits a less pronounced scattering intensity than Pt. This difference can be attributed to the distinct atomic numbers and electron densities of Ag and Pt metals.

Within the framework of BNP synthesis on surfaces, it is important to acknowledge the complex interplay of factors influencing their formation and structure. The deposition of two distinct metals introduces a multifaceted system where each element exhibits unique characteristics, including surface mobility, evaporation rates, and adsorption/desorption kinetics. These intrinsic differences can lead to challenging growth dynamics and unexpected structural effects that differ from those of the monometallic components. The characteristic parameters of 50 : 50 AgPt BNPs, as shown in Table 1, consistently fall between those of Ag and Pt monometallic counterparts. This intermediate behavior provides strong evidence for successful nanoalloying, rather than the formation of segregated monometallic domains.

Modifying the Ag : Pt ratio does not lead to significant changes in the overall structural characteristics of the nanocomposite, as confirmed by our GISAXS simulations (Fig. S3†). A 50 : 50 Ag : Pt composition was selected as the baseline for this study based on both thermodynamic and practical considerations.

First, this near-equimolar ratio aligns with the formation of a stable L_{11} ordered alloy phase, as suggested by the Ag–Pt binary phase diagram,[52] which minimizes the risk of phase separation commonly observed at other stoichiometric ratios. Compositions with a higher Ag content tend to exhibit phase separation, reduced thermal stability, and diminished plasmonic–catalytic synergy due to weaker Ag–Pt bonding and Ag surface segregation.

Second, our use of UHV atomic vapor deposition provides precise control over metal fluxes, enabling accurate tuning of the Ag : Pt ratio. The 50 : 50 composition represents an optimal balance between the high plasmonic response of Ag and the superior chemical and thermal stability of Pt. This provides a solid foundation for exploring the interplay between plasmonic enhancement and long-term stability in these nanocomposites.

The optimization of NP synthesis revealed a critical concentration threshold of $(5.2 \pm 0.3) \times 10^{15}$ atoms per cm^2, which yields a uniform, densely packed monolayer of NPs with minimal interparticle distances and low size dispersity. Subthreshold concentrations result in sparse distributions of ultrasmall NPs, predominantly below 1 nm in diameter. Conversely, exceeding this concentration induces extensive particle aggregation and high polydispersity. These findings were corroborated by GISAXS analysis, which confirmed 5.2×10^{15} atoms per cm^2 as the optimal concentration for achieving the desired nanoparticle characteristics. For effective plasmonic property characterization, several key parameters must be considered. Firstly, NP sizes were maintained above 1 nm to

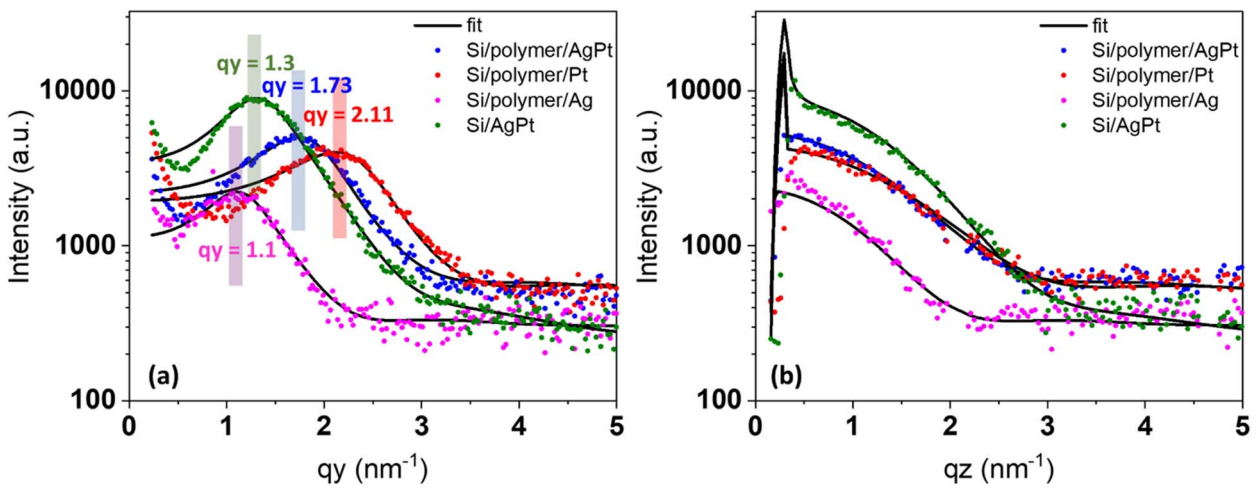

Fig. 3 (a) In-plane (q_y) and out-of-plane (q_z) GISAXS scattering profiles of mono- and bimetallic NPs derived from equivalent atomic deposition ($(5.2 \pm 0.3) \times 10^{15}$ atoms per cm^2) at RT: measured data (symbols) and theoretical fits (continuous lines) illustrating the polymer matrix and nanoalloying influence. Table 1 summarizes the structural parameters extracted from the q_y and q_z GISAXS profiles. The in-plane component, q_y, is sensitive to the nanoparticle diameter and interparticle distances, while the out-of-plane component, q_z, primarily reflects the height aspect ratio of the NPs.

ensure compatibility with the optical characterization technique employed, which has a spectral resolution of 1–2 nm. Secondly, robust signal generation is ensured by sufficient surface coverage, small interparticle distances, and the absence of agglomeration.

AgPt nanoalloys possess a perfectly balanced stoichiometric composition containing ~50% Ag and ~50% Pt as confirmed by comprehensive XPS and RBS analyses. However, comprehensive structural evidence supporting the uniform alloying of AgPt nanoparticles is provided in Fig. S4,† based on high-angle annular dark field (HAADF) imaging and lattice parameter analysis. The decomposition of Ag 3d and Pt 4f scans into several contributions clarifies the alloying behavior of the NPs. The positions of these contributions are calibrated using the C 1s peak of C–C bonds in the polymer as a reference to ensure consistency and accuracy in the measurements. As shown in Fig. 4(a), the XPS analysis of the Ag 3d scan reveals two distinct spectral features at binding energies of 367.4 eV and 373.4 eV, corresponding to the Ag $3d_{5/2}$ and Ag $3d_{3/2}$ transitions, respectively. These peaks are characteristic of metallic silver (Ag^0) species.[53–55] The well-defined spin–orbit splitting of 6 eV between Ag $3d_{5/2}$ and Ag $3d_{3/2}$ components, along with the asymmetric shape of the peak profiles, further validates the metallic nature of silver.[53–55] The Ag 3d spectral signatures in Fig. 4(a) correlate favorably with those found in the monometallic system (Fig. 4(b)), exhibiting some Ag^0 loss features on the higher binding energy side of each spin–orbit component for Ag metal.

Platinum (Pt $4f_{7/2}$ and Pt $4f_{5/2}$ transitions) was detected in two different oxidation states, Pt^0 and Pt^{2+}. As seen in Fig. 4(c), the surface composition is dominated by Pt^0 species, characterized by a binding energy separation (ΔBE) of 3.3 eV, while a minor fraction (6%) of PtO oxides is present, exhibiting a ΔBE of 3.2 eV.[54,55] The Pt 4f scan results in BNPs (Fig. 4(c)) differ somewhat from those of the monometallic scan (Fig. 4(d)), showing a shift of −0.8 eV for the metallic state and a shift of −0.6 eV for the oxide state. This suggests that electron donation occurred from Ag to Pt upon nanoalloying in a bimetallic system, thereby altering the nanoalloy's electronic properties and affecting the d-band structure on the surface.[56–58] The higher electronegativity of Pt relative to Ag results in electron donation from Ag to Pt, rather than the reverse, explaining the negative shift observed in the Pt 4f scans, while no corresponding shift was recognized in the Ag 3d scans.

The most striking observation from the data comparison is the presence of Pt oxides coupled with the absence of Ag oxides, despite Ag typically being more susceptible to oxidation than Pt. Further tests, conducted with GISAXS, corroborated these findings. Platinum's stronger interaction with the polymer and higher activation energy result in reduced surface mobility

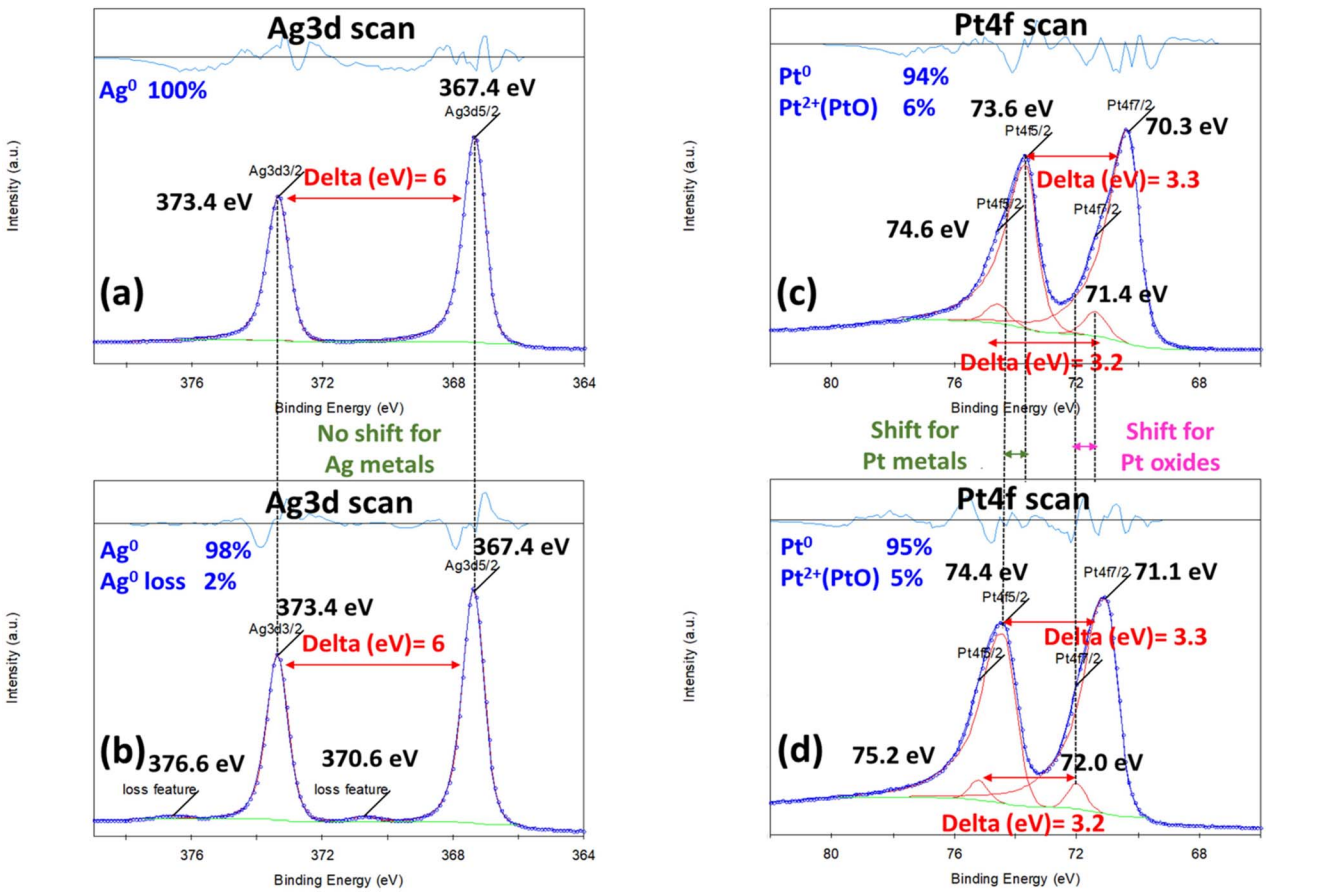

Fig. 4 Comparative high-resolution XPS spectra of Ag 3d and Pt 4f in single (b and d) and dual (a and c) metal systems.

compared to silver, as evidenced by smaller particle sizes and shorter interparticle distances as shown in Table 1. Platinum's partially filled 5d orbital ([Xe] $4f^{14}$ $5d^{9}$ $6s^{1}$) allows for better orbital overlap and hybridization with ligand orbitals, enabling stronger and more diverse bonding interactions with carboxylate groups in polymer diacrylates compared to silver's fully filled 4d orbital ([Kr] $4d^{10}$ $5s^{1}$). The presence of these oxides on freshly prepared substrates suggests they are formed from interactions with the polymer surface rather than surface oxidation caused by air exposure.

Confinement of NPs in the polymer matrix: insights from real-time XPS measurements at RT under UHV

Extreme caution must be taken when choosing a polymer for nanoparticle embedding. It is generally accepted that a high % of unreacted monomers can impede and slow the embedding process by acting as a barrier between NPs and polymer chains. To prevent limitations in the conversion extent, unreacted monomers were minimized by decreasing polymer functionality, viscosity, and cross-link density. This approach involved using a diacrylate polymer, which successfully confines NPs without requiring any post-treatment or additional processing steps.

Fig. 5 provides evidence for the diffusion and embedding of the NPs inside the polymer matrix, as demonstrated through surface-sensitive XPS with a depth of analysis of 10 nm. The XPS spectra presented in Fig. 5 were acquired under UHV conditions (10^{-10} mbar), using an uninterrupted vacuum transfer system from sample preparation to analysis. This protocol effectively eliminates any exposure to ambient air, thereby preventing the formation of a carbon contamination layer. The evolution of the high-resolution C 1s peak was monitored throughout a real-time analysis. The results in Fig. S5† confirm that carbon contamination was negligible, with no significant changes in the C 1s peak intensity or position observed throughout the real-time measurement. These observations support the stability of the surface chemistry and confirm that the data reflect intrinsic surface composition, not artifacts from atmospheric exposure.

In the initial stage of the process, when freshly prepared substrates were analyzed at RT under UHV, both Ag 3d and Pt 4f signals were detected on the surface with high sensitivity. Over time, a significant decrease in the intensity of these peaks was observed, becoming mostly negligible 12 days after synthesis. This reduction in intensity is attributed to the decreasing surface concentration of Ag and Pt over time, as the NPs diffused and embedded within the polymer matrix, beyond the 10 nm analysis depth.

Several factors likely influenced these results. The primary cause of embedding is thermodynamic factors, favoring the minimization of interfacial energy between NPs and the polymer. The surface energy of the polymer ($\gamma_{polymer} = 0.035$ J m^{-2})[59] is lower than that of Ag ($\gamma_{Ag} = 1.25$ J m^{-2})[60] and Pt ($\gamma_{Pt} = 2.48$ J m^{-2})[60] metals, creating a strong driving force for NPs to embed deeper into the polymer.[1,61,62] Nanoparticle confinement within polymer matrices is fundamentally governed by thermodynamic principles, with the work of adhesion (W_a) serving as a key parameter in determining the stability and distribution of nanoparticles within the host polymer. The work of adhesion quantifies the energetic favorability of the interface between the nanoparticle and the polymer; a positive W_a indicates that the interaction is favorable and drives the nanoparticle to embed within the polymer, thereby minimizing the interfacial Gibbs

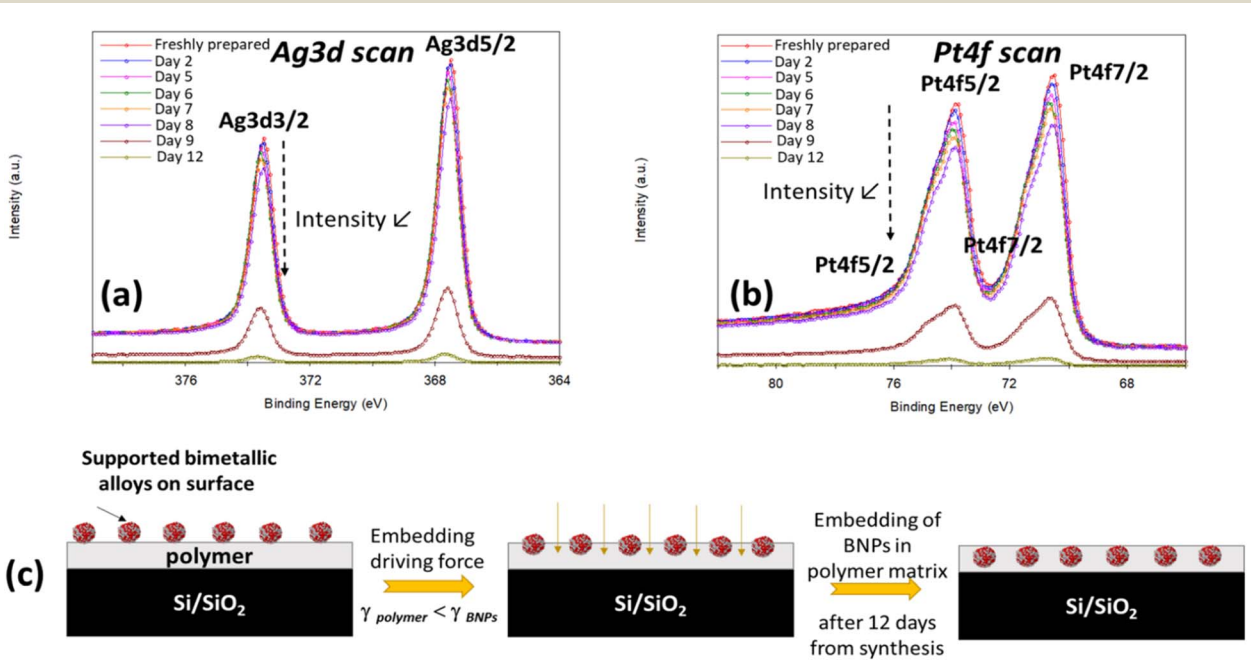

Fig. 5 Time-dependent XPS observations showing the temporal changes in (a) Ag 3d and (b) Pt 4f signals during nanoparticle diffusion and embedding in a polymer matrix at RT, and (c) a schematic view of the embedding stages in the polymer (the incident intensity of X-rays remained constant).

free energy (ΔG) and stabilizing the composite system. For instance, copper nanoparticles ($\gamma_{Cu} \approx 1.49$ J m^{-2}) can readily embed into poly(methyl methacrylate) ($\gamma_{PMMA} \approx 0.04$ J m^{-2}) due to the significant difference in surface energies, which creates a strong thermodynamic driving force for encapsulation. This process is further influenced by entropic factors, such as changes in polymer chain mobility and conformational entropy near the nanoparticle surface, but the overall effect is dictated by the balance of surface energies and the resulting work of adhesion.[63] In addition, it cannot be ignored that smaller NPs, within the range of our obtained sizes (~2–3 nm), have high surface energy per unit volume, making them more prone to embedding. The confinement process is size-dependent, smaller NPs (<12 nm) experience dominant capillary forces over elastic resistance that facilitate deep penetration into the polymer matrix, whereas larger NPs (>20 nm) face kinetic barriers due to the need for elastic deformation of polymer chains to form accommodating voids.[63] It is worth noting that the polymer's inherent mobility and softness, given that RT is above its glass transition temperature (T_g) which falls within a range of −47 °C to −30 °C,[64] are also prerequisites for accommodating NPs at their interface. Additionally, when the system at RT exceeds the polymer's T_g, the polymer transitions from a glassy to a rubbery state, allowing for localized chain rearrangement and further promoting nanoparticle embedding.[63]

Structural and optical properties

Extended studies using different imaging techniques (referenced in Fig. 6 and S6†) confirm our earlier findings presented in Fig. 5. These combined approaches yield visual confirmation of the nanoparticle incorporation within the polymer matrix.

The superior resolution of TEM provides precise information regarding the size, morphology, and interparticle distances of NPs, surpassing the capabilities of SEM. However, TEM lacks depth sensitivity, making it challenging to determine whether NPs are on the surface or embedded within the polymer matrix.

A closer inspection of the TEM micrographs, as depicted in Fig. 6(a), shows that the BNPs exhibit a quasi-spherical morphology. A minor fraction of these particles is interconnected, forming chain-like structures due to their proximity (static coalescence).[65] The particle population exhibits a monomodal size distribution. In our quantitative assessment, these chain-like formations are treated as single, connected NPs. A uniform distribution of Ag–Pt BNPs predominates on the surface, showing slight aggregation and low polydispersity while maintaining a high concentration of NPs on the support material. This can be explained by the large surface area and numerous functional groups of the polymer, which facilitate better dispersion and integration of the BNPs on the polymer film. Accordingly, the polymer serves as an ideal matrix for the homogeneous distribution of BNPs.

Comparatively, monometallic Ag and Pt NPs were assessed under identical experimental conditions, ensuring equivalent atomic deposition quantities. Interestingly, these monometallic samples exhibit morphologies similar to those of the bimetallic

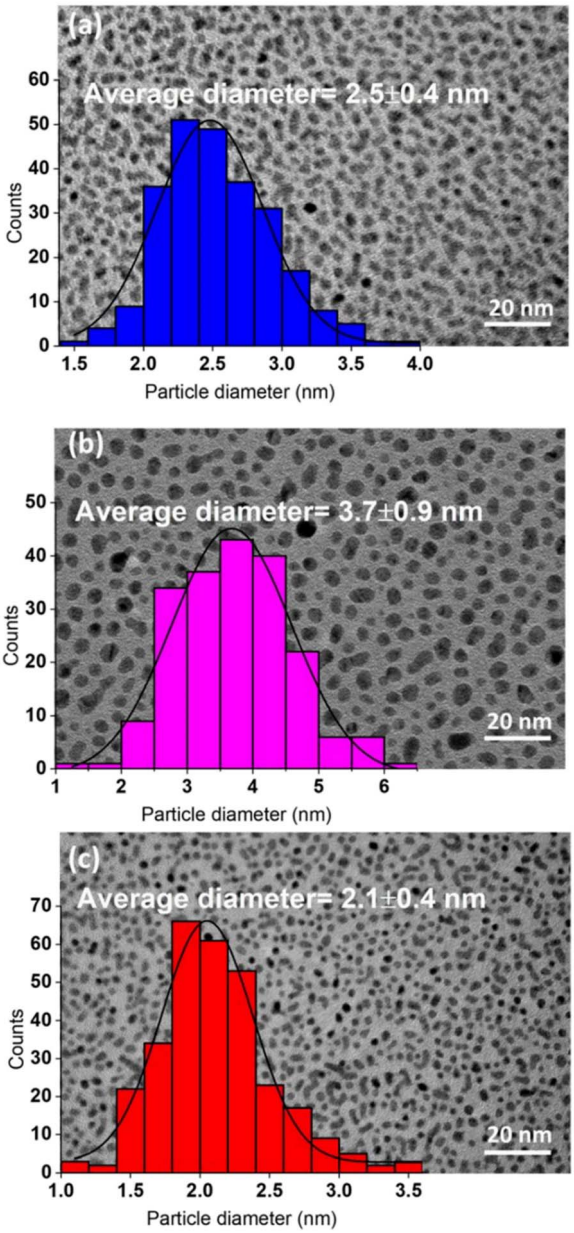

Fig. 6 Comparative TEM analysis of bimetallic and monometallic nanoparticles on polymer substrates. (a) Bimetallic AgPt nanoalloys, (b) monometallic Ag, and (c) monometallic Pt nanoparticles deposited on polymer layers. The insets show the corresponding particle size distribution histograms for each sample with their average diameter and standard deviation.

ones. AgNPs (Fig. 6(b)) exhibit greater heterogeneity in size and interparticle distances compared to AgPt nanoalloys (Fig. 6(a)) and PtNPs (Fig. 6(c)), with lower particle densities being observed.

A strong correlation is observed between the structural parameters obtained from GISAXS simulations and those derived from experimental TEM analysis, as detailed in Table 1 and visualized in Fig. 6. This correlation is particularly significant given the inherent differences in sampling between the two techniques. TEM provides localized information based on

a limited number of nanoparticles in specific regions, whereas GISAXS offers ensemble-averaged data from the entire film, leading to wider-area detection. In addition, differences in roughness values can be expected, which influence the diffusion and orientation of atoms and particles on the surface. In GISAXS, the high roughness ($R_q = 2$ μm) on the polymer surface leads to diffuse scattering of the beam, particularly at small angles of incidence, resulting in a large projected footprint. In contrast, for TEM analysis, the polymer thickness must be reduced to less than 100 nm to enhance contrast and NP visibility. This thickness reduction minimizes the expectation of significant roughness on the TEM carbon-coated membrane.

A notable feature of our spectroscopic analysis, as shown in Fig. 7, is its high sensitivity in detecting optical responses from NP monolayers on the substrate surface. However, the interpretation of these signals was challenging, as the expected well-defined standard peaks were absent. This complexity arises from several factors. First, the use of an opaque substrate necessitated reflection-based techniques rather than standard transmission measurements. Additionally, the highly reflective interior of the integrating sphere, essential for its function, introduced substantial background reflections. This effect was particularly pronounced for the small NPs in our study, which exhibit weak scattering properties. Consequently, the background signal often obscures the subtle optical response from the NP samples, resulting in a challenging signal-to-noise ratio.

The bimetallic AgPt nanoalloy system exhibits a single UV LSPR band centered at approximately 326 nm, as shown in Fig. 7(a). This band is spectrally positioned between those of pure Ag (~415 nm, Fig. 7(b)) and Pt (~275 nm, Fig. 7(c)) NPs. The absence of dual plasmonic peaks in the absorbance spectra of AgPt nanoalloys indicates the formation of alloy NPs, rather than a physical mixture of discrete Ag and Pt nanostructures. The presence of a single resonance peak also suggests high structural symmetry in the majority of the NPs. Additionally, the nanoscale dimensions of the particles rule out the possibility of quadrupolar modes, thereby eliminating the potential for dual-band occurrences.

AgPt BNPs exhibit enhanced LSPR through synergistic effects resulting from the interplay between Ag and Pt. The enhancement mechanism is governed by a combination of plasmonic, electronic, and interfacial phenomena. Ag provides a dominant LSPR response due to its highly favorable dielectric properties, characterized by a strongly negative real permittivity (ε_r) and a low imaginary component (ε_i). These attributes result in high-quality factor (Q-factor) resonances within the visible spectral range, making Ag a highly efficient plasmonic material.[20]

Although Pt is inherently less plasmonically active due to pronounced interband transitions, its incorporation into the alloy modifies the electronic structure of the nanoparticles. The d-band hybridization between Ag and Pt leads to reduced plasmon damping and a shift in resonance peak positions. This electronic coupling is particularly evident in fully alloyed AgPt nanoparticles, where the absorption band is modulated and stabilized within the 275–415 nm range.

Furthermore, interfacial charge redistribution at the Ag–Pt boundary results in the formation of localized electromagnetic hotspots—regions of intense field enhancement. These hotspots, often located at interparticle junctions or compositional interfaces, significantly amplify the near-field response and play a critical role in plasmon-enhanced applications such as SERS.[20]

It is noteworthy that the peak at 294 nm in Fig. 7(b) is associated with the polymer film, as previously discussed in Fig. 2(c). The appearance of the polymer's absorption peak at 294 nm in the UV-Vis spectrum of the Ag/polymer composite is attributed to the relatively low density of Ag nanoparticles (10×10^{11} NPs per cm^2, Fig. S8(h)†), in contrast to the significantly higher nanoparticle densities observed in the AgPt (87×10^{11} NPs per cm^2, Fig. 9(h)) and Pt (104×10^{11} NPs per cm^2, Fig. S7(h)†) samples. The reduced nanoparticle loading in the Ag sample results in less surface scattering, allowing more light to penetrate the polymer matrix and interact with its electronic structure. Consequently, the characteristic polymer absorption becomes visible in the Ag composite, while in the Pt and AgPt samples, this signal is obscured by the dominant scattering from their densely packed nanoparticle layers. The nanoparticle density obtained from GISAXS spectra follows a descending order: PtNPs (Fig. S7(h)†), AgPt nanoalloys (Fig. 9(h)), and AgNPs (Fig. S8(h)†). This result agrees with the peak intensity evolution observed in the absorbance spectra shown in Fig. 7.

The absence of the more intense C=O-related peak in UV-Vis reflection spectroscopy, despite its presence in ellipsometry, can be explained by the fundamental differences between these techniques. Ellipsometry, which relies on the phase-sensitive detection of polarized light, offers enhanced sensitivity to subtle

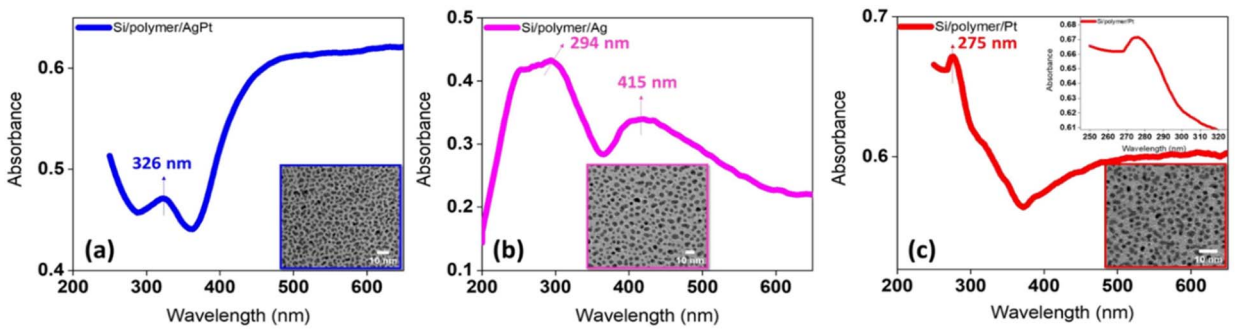

Fig. 7 UV-Vis absorption profiles of polymer-embedded nanoparticles on Si with equivalent atomic amount and the corresponding TEM micrographs in their insets: (a) AgPt nanoalloys, (b) Ag, and (c) Pt. Spectra were recorded using an integrating sphere in the reflection mode.

electronic transitions at interfaces. This allows it to resolve both the π–π* transition of C=C bonds (290 nm) and the n–π* transition of C=O groups (357 nm). In contrast, conventional UV-Vis reflection spectroscopy is based on intensity measurements and is less sensitive to weaker transitions. The n–π* transition of the C=O group has a relatively low absorption coefficient and is further masked by strong light scattering from the nanoparticle layer, making it undetectable in the UV-Vis spectra.

Ellipsometric data thus provide valuable confirmation of the polymerization process: the diminishing C=C peak reflects bond consumption, while the persistent C=O signal indicates retention of the carbonyl functionality throughout the reaction. To assess the long-term stability of the bimetallic sample on the polymer surface, we conducted a follow-up analysis of its plasmonic behavior seven months post-synthesis. The results, presented in Fig. 8(a), demonstrate remarkable consistency, with no discernible shift in the peak position and preservation of the original peak intensity. This preservation of spectral characteristics strongly indicates the sample's durability and its ability to maintain its unique optical properties over extended periods. In contrast, Fig. 8(b) reveals a significant difference in the plasmonic response of AgPt nanoalloys deposited on Si/SiO_2 surfaces. The characteristic peak at 330 nm was notably absent after seven months of air exposure, coupled with a marked reduction in the overall intensity. This big difference in long-term stability between the polymer-supported and Si/SiO_2-supported samples highlights the crucial influence of the substrate material on preserving the plasmonic properties of bimetallic nanostructures.

Our findings are consistent with previously reported data for AgPt solid solution nanoalloys, despite differences in synthesis methods. In a comparable study, 50 : 50 AgPt nanoalloys with mean diameters below 3 nm, synthesized *via* co-sputtering onto liquid polyethylene glycol (PEG), exhibited an absorption peak at ~350 nm. Additionally, this study reported absorption peaks at ~280 nm and ~400 nm for monometallic Pt and Ag NPs, respectively.[7] These spectral features align well with our observations, with slight deviations likely due to the higher density of NPs on the surface and their smaller interparticle distances. According to Mie theory simulations, spherical Ag NPs with a diameter of 3 nm embedded in a silica matrix are predicted to exhibit an absorption cross-section peak around 410 nm.[29] Given that the refractive index (RI ~ 1.5) of silica is comparable to that of many polymers, this theoretical prediction is relevant for similar polymer-based nanocomposite systems. Laser-synthesized colloidal Pt NPs, with a diameter of 2.7 nm suspended in deionized water, display a characteristic UV absorption peak at 245 nm.[66] When transitioning from an aqueous medium to a high refractive index polymer surface, the local dielectric environment surrounding the NPs changes significantly, resulting in a red shift of approximately 30 nm in the peak position due to modifications in electron oscillation frequency within the Pt NPs.

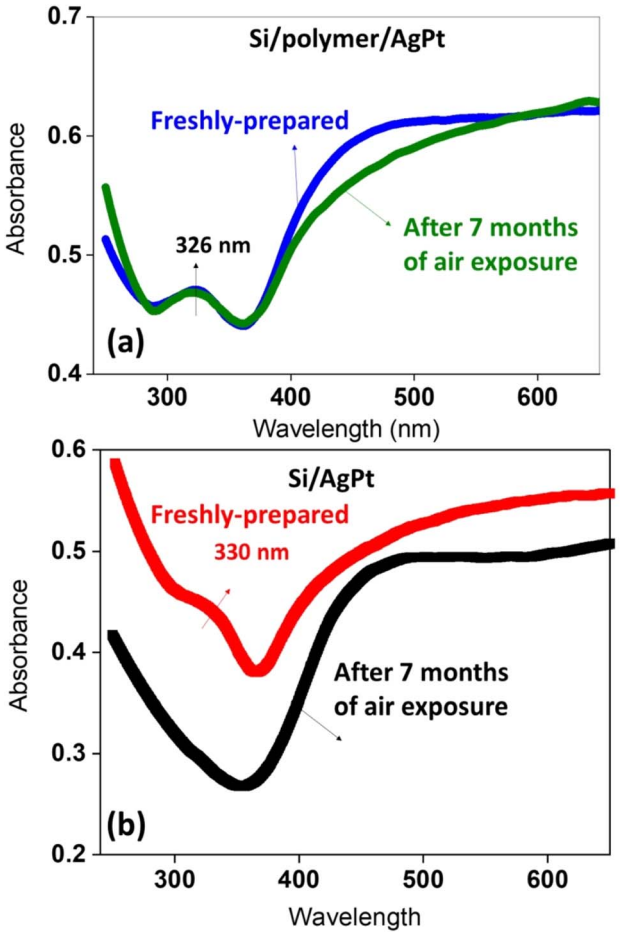

Fig. 8 UV-Vis absorption profiles of (a) polymer-embedded AgPt nanoalloys and (b) AgPt nanoalloys on Si/SiO_2, showcasing the initial profile immediately post-synthesis and the profile after 7 months of ambient air exposure.

Temperature-driven evolution of AgPt bimetallic nanostructures: a systematic annealing study

GISAXS measurements were performed at RT and at various annealing stages to evaluate the impact of post-deposition thermal treatment on the bimetallic sample. The annealing process involved heating from RT to 320 °C, with increments of 50 °C or 100 °C. The heating rate was maintained at 5 °C min^{-1}, and each stage lasted between 7 and 16 hours. The annealing procedure was executed over a total duration of two and a half days, ensuring thorough thermal treatment and allowing for detailed structural analysis at each stage. Fig. 9(a–f) present the GISAXS 2D patterns along with the corresponding scattered intensity profiles along both q_y and q_z. Detailed GISAXS simulation methodology can be found in the Experimental section in the ESI.† In the local monodisperse approximation (LMA), a polydisperse system is modeled as a collection of monodisperse elementary domains, where the total intensity is the incoherent sum of the scattered light from each domain. Multiple scattering effects across the surface were accounted for using the distorted wave Born approximation (DWBA).[50] To achieve a high q range and enable the investigation of finer structural details, a short sample-to-detector distance of 570 nm was chosen.

The temperature during growth induces high polydispersity in both size and spatial distributions, along with the formation of multiple nucleation centers on the surfaces. This leads to the

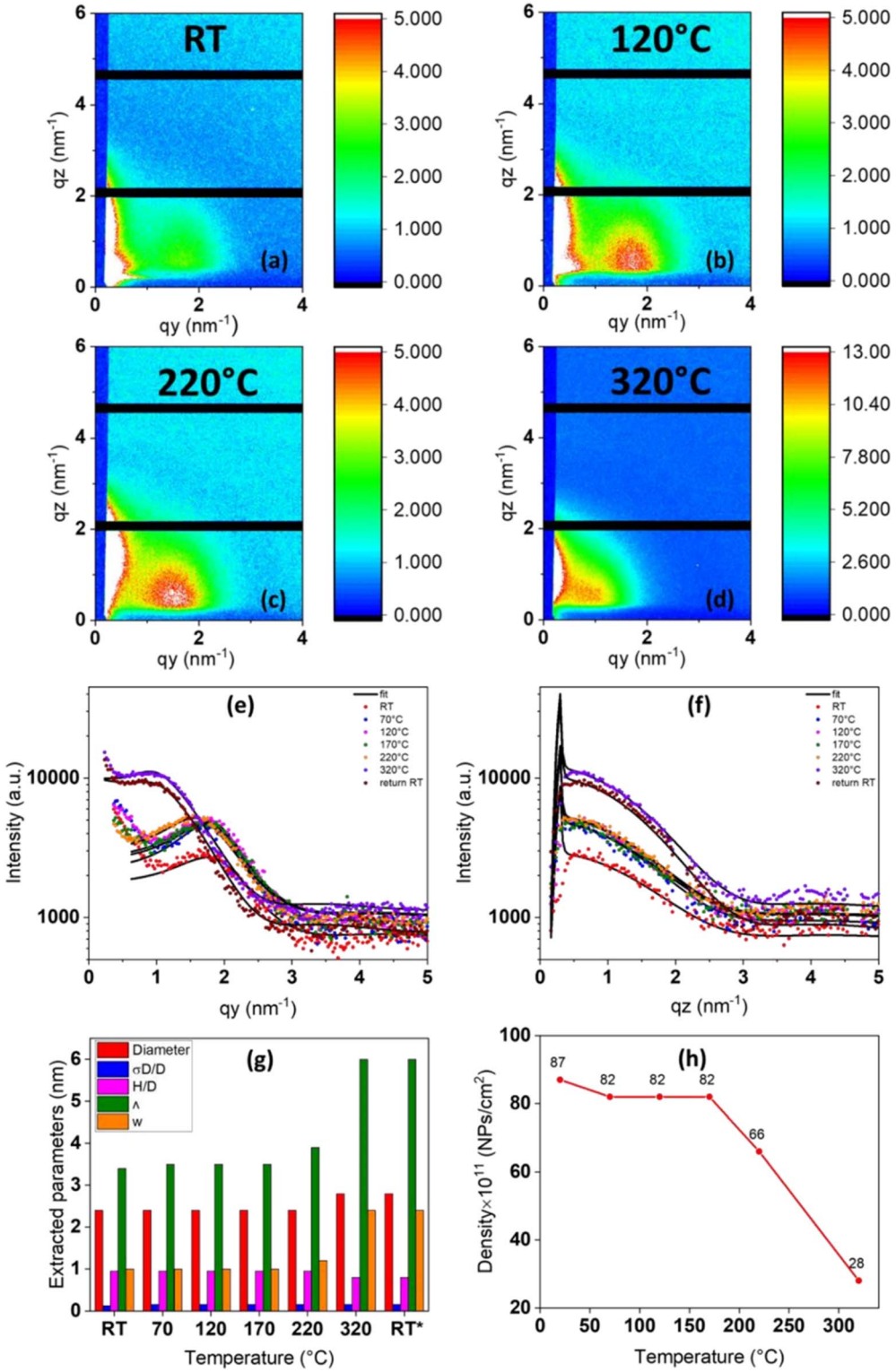

Fig. 9 GISAXS 2D patterns of Si/polymer/AgPt BNPs at different temperatures: (a) RT, (b) 120 °C, (c) 220 °C and (d) 320 °C, scattering intensity profiles with their corresponding fits (e) horizontally and (f) perpendicular to the substrate plane. (g) Quantitative analysis of particle characteristics and spatial distribution (diameter, σ_D/D, H/D, Λ, and w) from simulated data, and (h) the plot of the density of NPs *versus* temperature. RT* denotes the "Return to Room Temperature" phase after annealing.

development of smaller NPs as they grow across numerous nucleation sites. Consequently, modifying the diffusion mechanisms after NP formation was deemed preferable to better control the final nanostructure. This approach involved conducting the deposition process at RT, followed by subsequent thermal annealing steps.

Temperature significantly influences the surface diffusion, mobility, structural and morphological characteristics, composition, and size dispersion of NPs. AgPt BNPs fabricated by MBE initially exhibit a growth pattern consistent with the VW mode but in a metastable state at RT. In our case, NPs grow as discrete three-dimensional islands due to stronger metal–metal interactions compared to metal–substrate interactions. Despite the close lattice mismatch between Ag and Pt (approximately 4.1%) and their identical FCC crystalline structures, differences in cohesion (Ag: 2.96 eV per atom, Pt: 5.87 eV per atom),[60] surface energies (Ag: 1.25 J m^{-2}, Pt: 2.48 J m^{-2})[60] and the existence of the bulk miscibility gap favor the formation of equilibrium Pt-rich core/Ag-rich shell.[36] However, the literature frequently shows inverse core–shell VW growth[67] or mixing configurations due to strong kinetic or environmental effects at small sizes. Our observations in Fig. 9(g) show that annealing to 320 °C leads to the formation of isolated, compositionally mixed particles in a distribution at thermodynamic equilibrium. The primary objectives of annealing are: (i) to achieve an equilibrium state resistant to dynamic changes or transformations, and (ii) to facilitate the rapid incorporation of NPs into the polymer matrix. Fig. 9(g) shows the thermal threshold for atomic mobility activation and the onset of nanoparticle surface diffusion, indicating that a temperature above 220 °C is required to initiate these effects. According to Arrhenius's equation, there is a proportional relationship between temperature, diffusion coefficient, and mobility.[68] As the temperature exceeds 220 °C, the average NP diameter increases slightly from 2.4 to 2.8 nm, while the H/D ratio decreases from 0.95 to 0.8. Additionally, both Λ and w increase, all within a constant size distribution (σ_D/D).

Rising temperatures lead to a tendency towards anisotropic shapes (oblate), accompanied by a decrease in the H/D ratio. This suggests increased interaction between the NPs and the polymer support, likely due to higher interfacial adhesion energy.[40] The observed trends in all variables were consistent. At temperatures below 220 °C, the system predominantly consists of numerous closely spaced particles (ranging from 66 to 87 $\times$ 10^{11} NPs per cm^2), most of which are individually isolated with small distances ($\Lambda \sim 3.5$–3.9). In contrast, at 320 °C, the particle density significantly decreases to 28 $\times$ 10^{11} NPs per cm^2, leading to an increase in interparticle distances ($\Lambda \sim 6$). This inverse relationship between ρ and Λ is expressed as $\rho = 1/\Lambda^2$, with the density values as a function of temperature plotted in Fig. 9(h).

It is hypothesized that the polymer, PDGDA, has likely influenced the nanoalloy growth mechanism during annealing. PDGDA appears to control and limit the coalescence on the surface, effectively inhibiting extensive NP coalescence. This maintains small particle sizes and low dispersity in size distribution ($\sigma_D/D = 0.16$), even with prolonged annealing at elevated temperatures. The stabilizing environment provided by this polymer prevents NPs from approaching each other, thereby maintaining large interparticle distances.

The lack of changes in structural parameters upon returning to RT highlights the achievement of an equilibrium phase at 320 °C (Fig. 9(g)). The criterion for evaluating the equilibrium phase temperature is based on the stability of structural and morphological parameters rather than predetermined thresholds. The first degradation of PEGDA occurs around 370 °C, as confirmed by TGA analysis.[69] PDGDA is expected to decompose beyond 370 °C due to its stronger intermolecular forces, associated with additional carbon bonds. This confirms the robustness of the polymer under various temperature conditions. Overall, an equilibrium phase is attained without any deterioration in polymer properties.

Further details on monometallic Ag and Pt samples are provided in the ESI (Fig. S8 and S9).†

Annealing effectively facilitates the embedding of NPs in the polymer matrix, as shown in Fig. 10. These results show significant promise in reducing and accelerating the time required for NP confinement. Previously, a 12-day period at RT was necessary for satisfactory confinement, as shown in Fig. 5. However, the annealing process significantly accelerates this embedding process, as indicated by the rapid drop in the intensity of Ag 3d and Pt 4f scans. Following annealing, NPs immediately embed within the polymer matrix.

Heating enhances the kinetic energy of the polymer molecules, increasing their mobility and causing the polymer chains to vibrate more vigorously and move more freely. This elevated temperature weakens intermolecular forces between polymer chains and expands the free volume within the polymer matrix, reducing cohesive forces and enhancing chain flexibility. Consequently, transient voids and diffusion pathways form,

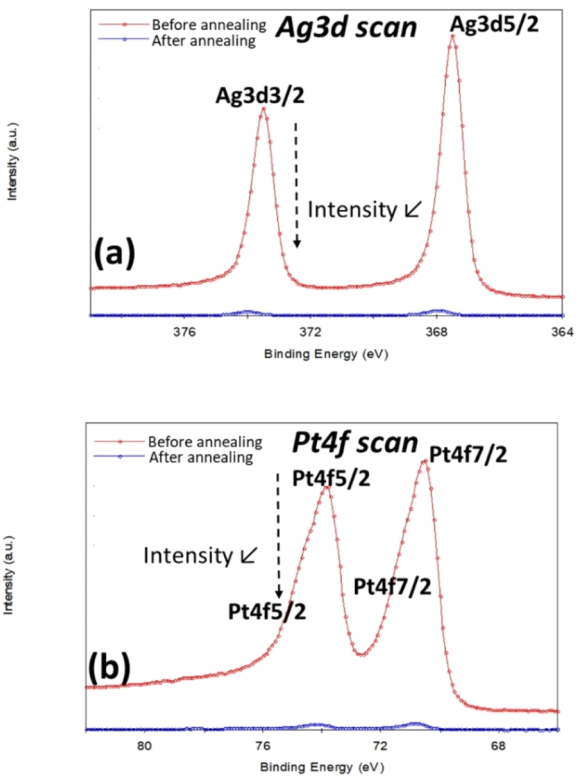

Fig. 10 XPS Analysis of Ag 3d and Pt 4f signals revealing nanoparticle dynamics in the polymer matrix: pre- and post-annealing observations.

facilitating the embedding of the NPs into the polymer matrix. The overall effect is a reduction in the polymer's viscosity, facilitating the movement of NPs through the matrix.

Conclusions

In this paper, the development of an original methodology leading to the incorporation of structure-controlled AgPt nanoalloys, with sizes ranging from 2 to 3 nm, into a PDGDA matrix system, was demonstrated. By synergistically employing photochemical techniques and electron beam evaporation, we have successfully fabricated a polymer nanocomposite material that shows high stability and durability. This integration preserves the unique structural and plasmonic properties of the AgPt nanoalloys under ambient conditions and through various annealing stages. A key strength of our work is its potential adaptability to more complex configurations, such as Janus and core/shell nanostructures, which will be explored in future studies.

Our results demonstrate a strong correlation between GISAXS and TEM observations, affirming the robustness of our approach. Additionally, the use of an integrating sphere in combination with UV-Vis spectrophotometry has proven effective in overcoming challenges associated with nanoparticle analysis on non-transparent substrates. Notably, we have observed ultraviolet plasmonic behavior in the AgPt nanoalloys, marking a significant advancement beyond the conventional plasmonic response observed in the Vis-NIR of many nanomaterials. This discovery opens new avenues for the development of UV-based plasmonic devices, with promising applications in fields such as UV sensing, photocatalysis, and optoelectronics.

Data availability

The findings supporting this article, with detailed characterization techniques, have been included as part of the ESI.† Access to additional project data is governed by contractual agreements specific to the relevant region (French regional council, Centre Val de Loire R-CVL).

Author contributions

Conceptualization, investigation, methodology, visualization, data curation, writing—original draft preparation, and formal analysis: A. F.; conceptualization, supervision, project administration, investigation, review, and editing: P. A.; investigation and validation: C. A.; investigation, validation: C. M.; investigation, validation, methodology: L. B.; investigation and validation: D. Z. All authors have read and approved the final version of the manuscript for publication.

Conflicts of interest

There are no conflicts to declare.

Acknowledgements

This work was funded by French regional council Centre Val de Loire R-CVL (project call APR-IA), whose support was instrumental during the initial stages of the research. The authors acknowledge the technical staff of the ICMN instrumental platform (XPS and GISAXS), in particular Eric Bourhis and Nicolas Gouillon for technical help. We would like to extend our sincere appreciation to Prof. Christophe Sinturel for his fruitful discussions on ellipsometry. RBS experiments were done at CEMHTI laboratory, Orleans, France. This work was supported by the international research network IRN Nanoalloys of CNRS.

References

1 J. Prakash, J. C. Pivin and H. C. Swart, Noble metal nanoparticles embedding into polymeric materials: From fundamentals to applications, *Adv. Colloid Interface Sci.*, 2015, **226**, 187–202.

2 L. Tamayo, H. Palza, J. Bejarano and P. A. Zapata, Polymer composites with metal nanoparticles: synthesis, properties, and applications, in *Polymer Composites with Functionalized Nanoparticles*, Elsevier, 2019, pp. 249–286, [Internet]. [cited 2024 Oct 18], Available from: **https://www.sciencedirect.com/science/article/pii/B9780128140642000081**.

3 F. Mares-Briones, A. Higareda, J. L. Lopez-Miranda, R. Mendoza-Cruz and R. Esparza, Bimetallic AgPt nanoalloys as an electrocatalyst for ethanol oxidation reaction: synthesis, structural analysis, and electro-catalytic activity, *Nanomaterials*, 2023, **13**(8), 1396.

4 J. Wang, L. Guo, B. Pan, T. Jin, Z. Li, Q. Tang, *et al.*, Plasmon-driven methanol oxidation on PtAg nanoalloys prepared by improved pulsed laser deposition, *Faraday Discuss.*, 2023, **242**, 499–521.

5 A. Fahes, A. E. Naciri, M. Navvabpour, M. B. Shoker, S. Jradi and S. Akil, Anisotropic Ag@ Au architectures through real-time surface-based strategy of synthesis: Large-area enhanced nanosensors, *Sens. Bio-Sens. Res.*, 2022, **38**, 100528.

6 M. Ahmad, T. Nawaz, M. A. Assiri, R. Hussain, I. Hussain, M. Imran, *et al.*, Fabrication of Bimetallic Cu–Ag Nanoparticle-Decorated Poly(cyclotriphosphazene- *co* -4,4′-sulfonyldiphenol) and Its Enhanced Catalytic Activity for the Reduction of 4-Nitrophenol, *ACS Omega*, 2022, **7**(8), 7096–7102.

7 M. Zhu, M. T. Nguyen, Y. Chau, R. ting, L. Deng and T. Yonezawa, Pt/Ag Solid Solution Alloy Nanoparticles in Miscibility Gaps Synthesized by Cosputtering onto Liquid Polymers, *Langmuir*, 2021, **37**(19), 6096–6105.

8 E. Ehret, E. Beyou, G. V. Mamontov, T. A. Bugrova, S. Prakash, M. Aouine, *et al.*, Bimetallic PdAg nanoparticle arrays from monolayer films of diblock copolymer micelles, *Nanoscale*, 2015, **7**(31), 13239–13248.

9 J. Haemers, D. Zanghi, E. Le Bec, C. Genevois, S. Hajjar-Garreau and L. Balan, Plasmon Active Functional Coatings with Hybrid Bimetallic Nanoparticles@Polymers by

a Single Step Photoinduced Approach, *ACS Appl. Opt. Mater.*, 2024, **2**(1), 199–210.
10 T. Xu and Z. Geng, Strategies to improve performances of LSPR biosensing: Structure, materials, and interface modification, *Biosens. Bioelectron.*, 2021, **174**, 112850.
11 E. Petryayeva and U. J. Krull, Localized surface plasmon resonance: Nanostructures, bioassays and biosensing—A review, *Anal. Chim. Acta*, 2011, **706**(1), 8–24.
12 N. Hooshmand and M. A. El-Sayed, Collective multipole oscillations direct the plasmonic coupling at the nanojunction interfaces, *Proc. Natl. Acad. Sci. U. S. A.*, 2019, **116**(39), 19299–19304.
13 R. Borah and S. W. Verbruggen, Silver–Gold Bimetallic Alloy versus Core–Shell Nanoparticles: Implications for Plasmonic Enhancement and Photothermal Applications, *J. Phys. Chem. C*, 2020, **124**(22), 12081–12094.
14 Q. Zhang, T. S. Deng, Y. Q. Dou, M. Z. Wei, S. Li, J. Liu, *et al.*, Trimetallic Nanostructures of Silver–Platinum Alloy Shells on Gold Nanorods for Plasmon-Mediated Photocatalysis, *ACS Appl. Nano Mater.*, 2022, **5**(11), 17048–17058.
15 N. Mandal, A. Das and R. S. Moirangthem, In-situ label-free optical biosensing with plasmonic enhanced ellipsometry using partially-embedded bimetallic Ag-Au alloy nanoparticles, *Sens. Actuators, B*, 2023, **379**, 133164.
16 X. Xie, M. A. Van Huis and A. Van Blaaderen, Morphology-Controlled Growth of Crystalline Ag–Pt-Alloyed Shells onto Au Nanotriangles and Their Plasmonic Properties, *J. Phys. Chem. C*, 2023, **127**(32), 16052–16060.
17 S. K. Jha, Z. Ahmed, M. Agio, Y. Ekinci and J. F. Löffler, Deep-UV Surface-Enhanced Resonance Raman Scattering of Adenine on Aluminum Nanoparticle Arrays, *J. Am. Chem. Soc.*, 2012, **134**(4), 1966–1969.
18 K. Shimanoe, S. Endo, T. Matsuyama, K. Wada and K. Okamoto, Localized surface plasmon resonance in deep ultraviolet region below 200 nm using a nanohemisphere on mirror structure, *Sci. Rep.*, 2021, **11**(1), 5169.
19 S. Link and M. A. El-Sayed, Size and Temperature Dependence of the Plasmon Absorption of Colloidal Gold Nanoparticles, *J. Phys. Chem. B*, 1999, **103**(21), 4212–4217.
20 M. Rycenga, C. M. Cobley, J. Zeng, W. Li, C. H. Moran, Q. Zhang, *et al.*, Controlling the Synthesis and Assembly of Silver Nanostructures for Plasmonic Applications, *Chem. Rev.*, 2011, **111**(6), 3669–3712.
21 J. Lermé, C. Bonnet, M. A. Lebeault, M. Pellarin and E. Cottancin, Surface Plasmon Resonance Damping in Spheroidal Metal Particles: Quantum Confinement, Shape, and Polarization Dependences, *J. Phys. Chem. C*, 2017, **121**(10), 5693–5708.
22 Z. Liu, B. Xu, Y. Cheng, M. Si, X. Chu, M. Sun, *et al.*, Spectral analysis of oxidation on localized surface plasmon resonance of copper nanoparticles thin film, *Spectrochim. Acta, Part A*, 2023, **303**, 123202.
23 A. Fahes, A. En Naciri, M. Navvabpour, S. Jradi and S. Akil, Self-assembled Ag nanocomposites into ultra-sensitive and reproducible large-area SERS-Active opaque substrates, *Nanomaterials*, 2021, **11**(8), 2055.
24 K. W. Wang, S. R. Chung, L. Y. Jang, J. F. Lee and T. P. Perng, Compositional Inhomogeneity of Pd70Ag30 Alloy Nanoparticles, 2003 [cited 2024 Oct 21]; Available from: **https://hero.epa.gov/hero/index.cfm/reference/details/reference_id/5323354**.
25 R. Calvo, A. Thon, A. Saad, A. Salvador-Matar, M. Manso-Silván, Ó. Ahumada, *et al.*, Size characterization of plasmonic nanoparticles with dark-field single particle spectrophotometry, *Sci. Rep.*, 2022, **12**(1), 17231.
26 E. G. Graham, C. M. Macneill and N. H. Levi-Polyachenko, Review Of Metal, Carbon And Polymer Nanoparticles For Infrared Photothermal Therapy, *Nano LIFE*, 2013, **03**(03), 1330002.
27 V. Coviello, D. Forrer and V. Amendola, Recent Developments in Plasmonic Alloy Nanoparticles: Synthesis, Modelling, Properties and Applications, *ChemPhysChem*, 2022, **23**(21), e202200136.
28 S. A. Lee and S. Link, Chemical Interface Damping of Surface Plasmon Resonances, *Acc. Chem. Res.*, 2021, **54**(8), 1950–1960.
29 É. Camus, M. Pellarin, N. Blanchard, O. Boisron, M. Hillenkamp, L. Roiban, *et al.*, Structural and optical characterization of nanoalloys mixing gold or silver with aluminium or indium: evolution under various reactive environments, *Faraday Discuss.*, 2023, **242**, 478–498.
30 N. H. Khdary, B. T. Almuarqab and G. El Enany, Nanoparticle-embedded polymers and their applications: a review, *Membranes*, 2023, **13**(5), 537.
31 L. Balan, R. Schneider and D. J. Lougnot, A new and convenient route to polyacrylate/silver nanocomposites by light-induced cross-linking polymerization, *Prog. Org. Coat.*, 2008, **62**(3), 351–357.
32 G. K. Dalapati, H. Sharma, A. Guchhait, N. Chakrabarty, P. Bamola, Q. Liu, *et al.*, Tin oxide for optoelectronic, photovoltaic and energy storage devices: a review, *J. Mater. Chem. A*, 2021, **9**(31), 16621–16684.
33 P. Andreazza, V. Pierron-Bohnes, F. Tournus, C. Andreazza-Vignolle and V. Dupuis, Structure and order in cobalt/platinum-type nanoalloys: from thin films to supported clusters, *Surf. Sci. Rep.*, 2015, **70**(2), 188–258.
34 F. Ait Hellal, C. Andreazza-Vignolle, P. Andreazza and J. Puibasset, Equilibrium structure and shape of Ag and Pt nanoparticles grown on silica surfaces: From experimental investigations to the determination of a metal–silica potential, *J. Chem. Phys.*, 2024, **160**(16), 164717.
35 P. Andreazza, A. Lemoine, A. Coati, D. Nelli, R. Ferrando, Y. Garreau, *et al.*, From metastability to equilibrium during the sequential growth of Co–Ag supported clusters: A real-time investigation, *Nanoscale*, 2021, **13**(12), 6096–6104.
36 J. Pirart, A. Front, D. Rapetti, C. Andreazza-Vignolle, P. Andreazza, C. Mottet, *et al.*, Reversed size-dependent stabilization of ordered nanophases, *Nat. Commun.*, 2019, **10**(1), 1982.
37 P. Andreazza, C. Mottet, C. Andreazza-Vignolle, J. Penuelas, H. C. N. Tolentino, M. De Santis, *et al.*, Probing nanoscale structural and order/disorder phase transitions of

supported Co-Pt clusters under annealing, *Phys. Rev. B: Condens. Matter Mater. Phys.*, 2010, **82**(15), 155453.
38 J. Plé, C. S. Stan, D. Zanghi, C. Genevois, S. Hajjar-Garreau and L. Balan, Photoinduced polymer-confined CQDs for efficient photoluminescent 2D/3D printing applications, *Mater. Adv.*, 2023, **4**(21), 5140–5148.
39 M. Jacquemin, M. J. Genet, E. M. Gaigneaux and D. P. Debecker, Calibration of the X-Ray Photoelectron Spectroscopy Binding Energy Scale for the Characterization of Heterogeneous Catalysts: Is Everything Really under Control?, *ChemPhysChem*, 2013, **14**(15), 3618–3626.
40 F. A. Hellal, Structure et cinétique de formation de nanoparticules bimétalliques à base d'argent et de platine déposées sur des supports en faible interaction, *PhD thesis*, Université d'Orléans, 2022, [cited 2024 Oct 21]. Available from: **https://theses.hal.science/tel-04046972/**.
41 L. S. Magalhães, D. B. Andrade, R. D. Bezerra, A. I. Morais, F. C. Oliveira, M. S. Rizzo, *et al.*, Nanocomposite hydrogel produced from PEGDA and laponite for bone regeneration, *J. Funct. Biomater.*, 2022, **13**(2), 53.
42 M. Imani, S. Sharifi, H. Mirzadeh and F. Ziaei, Monitoring of Polyethylene Glycol-diacrylate-based Hydrogel Formation by Real Time NMR Spectroscopy, *Iran. Polym. J.*, 2007, **16**(1), 13–20.
43 T. Şener Raman, M. Kuehnert, O. Daikos, T. Scherzer, C. Krömmelbein, S. G. Mayr, *et al.*, A study on the material properties of novel PEGDA/gelatin hybrid hydrogels polymerized by electron beam irradiation, *Front. Chem.*, 2023, **10**, 1094981.
44 T. N. Dharmapriya, H. Y. Shih and P. J. Huang, Facile synthesis of hydrogel-based ion-exchange resins for nitrite/nitrate removal and studies of adsorption behavior, *Polymers*, 2022, **14**(7), 1442.
45 T. N. Dharmapriya, D. Y. Lee and P. J. Huang, Novel reusable hydrogel adsorbents for precious metal recycle, *Sci. Rep.*, 2021, **11**(1), 19577.
46 A. Lasagni, D. Yuan, P. Shao and S. Das, Rapid fabrication of biocompatible hydrogels microdevices using laser interference lithography, in *Bioengineered and Bioinspired Systems IV*, SPIE, 2009, pp. 164–172, Available from: **https://www.spiedigitallibrary.org/conference-proceedings-of-spie/7365/73650I/Rapid-fabrication-of-biocompatible-hydrogels-microdevices-using-laser-interference-lithography/10.1117/12.821099.short**.
47 E. M. Kosower and J. R. de Souza, nπ-ct-π* Transitions: nπ* Transitions of the second kind, *Chem. Phys.*, 2006, **324**(1), 3–7.
48 C. J. Reckmeier, Y. Wang, R. Zboril and A. L. Rogach, Influence of Doping and Temperature on Solvatochromic Shifts in Optical Spectra of Carbon Dots, *J. Phys. Chem. C*, 2016, **120**(19), 10591–10604.
49 J. A. Venables, G. D. T. Spiller and M. Hanbucken, Nucleation and growth of thin films, *Rep. Prog. Phys.*, 1984, **47**(4), 399.
50 G. Renaud, R. Lazzari and F. Leroy, Probing surface and interface morphology with grazing incidence small angle X-ray scattering, *Surf. Sci. Rep.*, 2009, **64**(8), 255–380.
51 G. Y. Krasnikov, N. A. Zaitsev, I. V. Matyushkin and S. V. Korobov, Cellular automaton model of phase separation during annealing of nonstoichiometric silicon oxide layers, *Russ. Microelectron.*, 2015, **44**(8), 523–530.
52 M. H. F. Sluiter, C. Colinet and A. Pasturel, *Ab initio* calculation of the phase stability in Au-Pd and Ag-Pt alloys, *Phys. Rev. B: Condens. Matter Mater. Phys.*, 2006, **73**(17), 174204.
53 J. Wisniewska, I. Dziedzic and M. Ziolek, A platinum promoted Ag/SBA-15 catalyst effective in selective oxidation of methanol–design and surface characterization, *RSC Adv.*, 2020, **10**(25), 14570–14580.
54 M. C. França, R. M. Ferreira, F. Dos Santos Pereira, F. A. E Silva, A. C. A. Silva, L. C. S. Cunha, *et al.*, Galvanic replacement managing direct methanol fuel cells: AgPt nanotubes as a strategy for methanol crossover effect tolerance, *J. Mater. Sci.*, 2022, **57**(17), 8225–8240.
55 J. Bi, P. Gao, B. Wang, X. Yu, C. Kong, L. Xu, *et al.*, Intrinsic insight on localized surface plasmon resonance enhanced methanol electro-oxidation over a Au@ AgPt hollow urchin-like nanostructure, *J. Mater. Chem. A*, 2020, **8**(14), 6638–6646.
56 N. Sui, R. Yue, Y. Wang, Q. Bai, R. An, H. Xiao, *et al.*, Boosting methanol oxidation reaction with Au@ AgPt yolk-shell nanoparticles, *J. Alloys Compd.*, 2019, **790**, 792–798.
57 X. Jiang, G. Fu, X. Wu, Y. Liu, M. Zhang, D. Sun, *et al.*, Ultrathin AgPt alloy nanowires as a high-performance electrocatalyst for formic acid oxidation, *Nano Res.*, 2018, **11**(1), 499–510.
58 S. Varshney, R. Bar-Ziv and T. Zidki, On the Remarkable Performance of Silver-based Alloy Nanoparticles in 4-Nitrophenol Catalytic Reduction, *ChemCatChem*, 2020, **12**(18), 4680–4688.
59 U. De Rossi, O. Bolender and B. Domanski, Dynamic surface tension of UV-curable inkjet inks, in *NIP & Digital Fabrication Conference*, Society of Imaging Science and Technology, 2004, pp. 788–792, Available from: **https://library.imaging.org/print4fab/articles/20/1/art00058_2**.
60 J. Ruvireta Jurado, Coinage and Pt-group metal surfaces stability, 2016, [cited 2024 Oct 21]; Available from: **https://diposit.ub.edu/dspace/handle/2445/101280**.
61 X. Hu, D. G. Cahill and R. S. Averback, Burrowing of Pt nanoparticles into SiO 2 during ion-beam irradiation, *J. Appl. Phys.*, 2002, **92**(7), 3995–4000.
62 R. D. Deshmukh and R. J. Composto, Direct Observation of Nanoparticle Embedding into the Surface of a Polymer Melt, *Langmuir*, 2007, **23**(26), 13169–13173.
63 H. C. Bonde, P. Fojan and V. N. Popok, Controllable embedding of size-selected copper nanoparticles into polymer films, *Plasma Processes Polym.*, 2020, **17**(5), 1900237.
64 A. Priola, G. Gozzelino, F. Ferrero and G. Malucelli, Properties of polymeric films obtained from uv cured poly (ethylene glycol) diacrylates, *Polymer*, 1993, **34**(17), 3653–3657.
65 J. Penuelas, C. Andreazza-Vignolle, P. Andreazza, A. Ouerghi and N. Bouet, Temperature effect on the ordering and

morphology of CoPt nanoparticles, *Surf. Sci.*, 2008, **602**(2), 545–551.

66 R. A. Ganeev, M. Suzuki, M. Baba, M. Ichihara and H. Kuroda, Low-and high-order nonlinear optical properties of Au, Pt, Pd, and Ru nanoparticles, *J. Appl. Phys.*, 2008, **103**(6), 063102. Available from: **https://pubs.aip.org/aip/jap/article/103/6/063102/284384**.

67 Y. Fan, A. Girard, M. Waals, C. Salzemann and A. Courty, Ag@Pt Core–Shell Nanoparticles for Plasmonic Catalysis, *ACS Appl. Nano Mater.*, 2023, **6**(2), 1193–1202.

68 J. Chen, S. Liu, Q. Min, S. Huang, K. W. Richter, J. Hu, *et al.*, Interdiffusion and atomic mobility in FCC Ag–Cu–Ni alloys, *J. Mater. Res. Technol.*, 2024, **29**, 3795–3804.

69 S. Saimani and A. Kumar, Polyethylene glycol diacrylate and thermoplastic polymers based semi-IPNs for asymmetric membranes, *Compos. Interfaces*, 2008, **15**(7–9), 781–797.